Advances in Applied Mathematics and Mechanics
Adv. Appl. Math. Mech., Vol. **10**, No. 6, pp. 1497-1526

DOI: 10.4208/aamm.OA-2018-0005
December 2018

Particle Scale Numerical Simulation on Momentum and Heat Transfer of Two Tandem Spheroids: an IB-LBM Study

Chunhai Ke[1], Shi Shu[1], Hao Zhang[2,*] and Haizhuan Yuan[1]

[1] *Hunan Key Laboratory for Computation and Simulation in Science and Engineering, Xiangtan University, Xiangtan 411105, Hunan, China*
[2] *School of Metallurgy, Northeastern University, Shenyang 110819, Liaoning, China*

Received 2 January 2018; Accepted (in revised version) 10 May 2018

Abstract. The cold fluid flowing over two hot spheroids placed in a tandem arrangement was numerically studied via a GPU-based immersed boundary-lattice Boltzmann method (IB-LBM) model. The drag coefficient and average Nusselt number of both the two spheroids were obtained with the main influencing factors investigated. To validate the IB-LBM model, several numerical case studies containing one and two spheres were firstly conducted to reach the good agreement with the previously reported data. Then, a number of simulations were further carried out which were designed by changing the particle aspect ratio ($1.0 \leq Ar \leq 4.0$) and inter particle distance ($1.5 \leq \ell \leq 7.0$, where $\ell = L/D$, D stands for the volume-equivalent sphere diameter) as well as the Reynolds number ($10 \leq Re \leq 200$). Their influence on the momentum and heat transfer characteristics between the solid and fluid phases was fully discussed. Numerical results show that, for all the considered Reynolds numbers and aspect ratios, the individual and total drag coefficients and average Nusselt number increase with the inter particle distance. The inter particle distance has greater influence on the drag coefficient and average Nusselt number of the trailing particle than the leading one. The drag coefficient and average Nusselt number of the trailing particle are far less than the leading one under the same working conditions. The prediction correlations for the drag coefficient and average Nusselt number of both the two spheroids were established with low deviations. At last, the influence of the relative incidence angles between the two tandem spheroids on the momentum and heat transfer was studied. It is shown that the relative incidence angles play significant roles due to the change of the frontal area of the leading spheroid with these angles.

AMS subject classifications: 76T25, 68U20

Key words: Drag coefficient, average Nusselt number, IB-LBM, spheroids, inter particle distance, relative incidence angle.

---

*Corresponding author.
Email: zhangh@mail.neu.edu.cn (H. Zhang)

1 Introduction

1.1 Background

The fluid flowing over solid particles with different temperature is one of the most encountered phenomenon in both engineering applications and daily life. In these processes, the important information that people care about and use for the scaling design and configuration optimization of the current devices is the momentum and heat transfer between the two phases which are usually characterized by two dimensionless parameters, namely the drag coefficient (Cd) and average Nusselt number (Nu), respectively. Previous work has demonstrated that several important factors play key roles in influencing on Cd and Nu, such as the Reynolds number, particle shape with its orientation and surroundings [47]. Therefore, understanding the contribution of each factor and combining all these information to predict Cd and Nu accurately are of paramount importance to provide optimization policy on the operating parameters and energy efficiency.

Two spheroids in a tandem arrangement are a typical case of the afore-mentioned system to dig the mechanism governing the complex representations. In such cases, a tuning on the Reynolds number, aspect ratio, inter particle distance and relative incidence angle makes it possible to construct different working conditions and evaluate corresponding Cd and Nu, quantitatively. On the one hand, the leading particle exerts great influence on the force evolution and heat transfer of the second particle because of the inhibition to the fluid flow. On the other hand, due to the adjunction of the trailing particle, a significant effect is brought on the evolution of the recirculation wake of the leading particle especially when the inter particle distance between the two particles is very small. In the previous studies, the researchers have paid much attention on the momentum and heat transfer of an isolated particle and the drag force of two tandem spheroids. However, there is a gap left to describe how these factors affect the heat transfer characteristics of two tandem particles. Especially, the effect of the relative incidence angles between the two spheroids is mainly ignored before. All these facts motivate the current research.

1.2 Previous work

There have been many studies on the momentum and heat transfer for an isolated particle immersed in a fluid which have been reviewed in our previous paper [13]. Here, only a brief story is given followed by a detailed version on the two particle cases. Yuge [45] and Klyachko [19] carried out experimental studies on this topic at very small Reynolds and Grashof numbers followed by the study of Chen and Mucoglu [4] at higher Reynolds and Grashof numbers. Juncu [12] investigated the transient heat transfer from two types of spheroids to a steady stream of viscous flows. Hölzer and Sommerfeld obtained the drag, lift and moment coefficients of six kinds of particles with different shapes through numerical simulation [8]. The lattice Boltzmann method (LBM) simulations were conducted to simulate the fluid flow over various non-spherical particles and improve the accuracy of the existing correlations [7,13] for both the drag coefficient and average Nusselt number. Kishore and Gu [18] used the ANSYS Fluent package to examine the momentum and heat transfer phenomena of spheroids. Richter and Nikrityuk also solved the NS equations and proposed novel correlations of the drag coefficient and average Nusselt number based on the numerical results [30,31].

When the solid particle is not isolated, the flow and heat transfer characteristics could be highly influenced by the arrangement of the surrounding particles which calls for further investigations. Rowe and Henwood [33] and Tsuji et al. [40] experimentally measured the drag forces on a pair of spheres at $32 \leq Re \leq 96$ and $Re = 10^3$, respectively. Zhu et al. [48] reported the measurements of the drag forces on two interactive spheres at $Re < 200$. Liang et al. [22] focused on the effects of particle arrangements on the drag force of a particle at Reynolds numbers ranging between 30 and 106. The drag and fluid mechanic characteristics of an interactive sphere were experimentally studied by Chen et al. [2] and then the effects of the inter particle distance and the size of the surrounding sphere on the drag were also studied in their flowing work [3]. Kim et al. [15] investigated the velocities, turbulence intensities, Reynolds shear stresses and turbulent kinetic energies of the flow fields around two tandem square cylinders via an experimental method at $Re = 5300$ and 16000. Another experimental study was conducted by Wang et al. [42] to investigate the flow around two tandem square cylinders in a tandem arrangement and the effect of a plane wall was considered.

Besides the direct measurement based on the experimental tools, several numerical works were also reported. Tal et al. [35] numerically studied the momentum and heat transfer around a pair of tandem spheres at $Re = 40$ for two inter particle distances. The numerical results showed that the drag coefficient and average Nusselt number of either sphere is always less than that of an isolated sphere with the effect being much stronger on the downstream sphere. Chen et al. [1] studied the momentum and heat transfer characteristics of the fluid flow with two identical isothermal spheres in a tandem arrangement. Kim et al. [14] investigated the lift, moment and drag coefficients at Reynolds numbers 50, 100 and 150 for two identical spheres placed side by side. Tsuji et al. [39] numerically studied the flow interactions around two particles at Reynolds numbers 30, 100, 200 and 250, respectively. They concluded that the nozzle effect increases the drag for small gaps but is negligible for large ones. Juncu [10] presented a numerical study on the steady axisymmetric viscous flow around two tandem circular cylinders. The influence of the distance between the cylinders on the momentum transfer of the upstream cylinder was studied. Later, the heat transfer of the fluid flow from two circular cylinders in a tandem arrangement was presented by the same author [11]. Kishore [16] investigated the steady Newtonian flow over two tandem spheroids based on two-dimensional numerical simulations in which the effects of the Reynolds number, particle aspect ratio and inter particle distance were investigated. Then, the flow and drag phenomena of three tandem spheroids were studied in the following work [17]. Vu et al. [41] studied the flow past two circular cylinders in tandem and side-by-side arrangements at low Reynolds numbers with the effect of their distances discussed. In the work of Musong et al. [23], the free convection of a single sphere and small aggregates composed of groups of two and three spheres in a viscous Newtonian fluid was studied. Yoon and Yang [43] and Sohankar and Etminan [34] investigated the flow characteristics and heat transfer between the flows and two identical spheres and two equal square cylinders, respectively. Forced convection of an isolated and an in-line array of three spheres was investigated in the work of Tavassoli et al. [36]. Then, they presented the heat transfer coefficients (HTC) of bidisperse random arrays of spheres at the Reynolds number $30 \le Re \le 100$ pointing that the correlation of the monodisperse HTC can estimate the average HTC of bidisperse systems well if the Reynolds and Nusselt numbers are based on the Sauter mean diameter [38]. From a numerical study on the flow and heat transfer past two side-by-side spheres, Li et al. [21] found that as the gap ratio decreases, the average drag coefficients of both the spheres increase but the average Nusselt numbers do not change much. The local Nusselt number variation on the surfaces varies greatly as the gap ratio changes. Kruggel et al. [20] studied the coupled fluid flow and heat transfer for a single particle and particle packings of random mono-disperse stationary particles by a LBM-approach.

1.3 Motivation and summary of the present work

From the literature survey, it can be seen that various studies for the momentum and heat transfer have been proposed for the single particles, especially for the spheres. The investigation on the two non-spherical particles configuration was mainly limited in 2D cases or cold modelling. The 2D simplification disables the consideration of the particle rotation and the cold modelling ignores the heat transfer. Therefore, the aim of this work is to fill this gap in the literature. In this work, the effects of the particle aspect ratio Ar, Reynolds number Re and inter particle distance between particle centers L on the drag and heat transfer of tandem spheroids are elucidated in the following range of conditions: $10 \le Re \le 200$, $1.0 \le Ar \le 4.0$ and $1.5D \le L \le 7.0D$ with two relative incidence angles θ and ϕ.

The rest of the paper is organized as follows. Section 2 briefly gives the mathematics of the LBM and immersed boundary method (IBM) [25]. Section 3 introduces the details of the numerical issue and calculation platform. In Section 4, validation simulations are carried out. In Section 5, 125 case studies are tested and new correlations for the drag coefficient and average Nusselt number are proposed based on the numerical results. The influence of the relative incidence angles on the momentum and heat transfer is also discussed. At last, main findings are summarized in Section 6.

2 Governing equations

2.1 Lattice Boltzmann method

In this study, we use the D3Q15 LBM model [27] to simulate the incompressible Newtonian fluid which is given as et al. [9]

$$\begin{cases} f_\alpha(\mathbf{r}+\mathbf{e}_\alpha\delta_t,t+\delta_t)=f_\alpha(\mathbf{r},t)-\dfrac{f_\alpha(\mathbf{r},t)-f_\alpha^{eq}(\mathbf{r},t)}{\tau_f}+F_\alpha\delta_t, \\ g_\alpha(\mathbf{r}+\mathbf{e}_\alpha\delta_t,t+\delta_t)=g_\alpha(\mathbf{r},t)-\dfrac{g_\alpha(\mathbf{r},t)-g_\alpha^{eq}(\mathbf{r},t)}{\tau_g}+G_\alpha\delta_t, \end{cases} \tag{2.1}$$

where $f_\alpha(\mathbf{r},t)$ and $g_\alpha(\mathbf{r},t)$ stand for the fluid density and internal energy distribution functions, respectively. The index α runs from 0 to 14 and the corresponding lattice velocities $\mathbf{e}_\alpha$ as shown in Fig. 1 read

$$\mathbf{e}_\alpha=\begin{cases} (0,0,0), & \alpha=0, \\ (\pm c,0,0),(0,\pm c,0),(0,0,\pm c), & \alpha=1,2,3,4,5,6, \\ (\pm c,\pm c,\pm c), & \alpha=7,8,9,10,11,12,13,14, \end{cases} \tag{2.2}$$

where c is the lattice speed. The superscript eq in Eq. (2.1) means equilibrium

$$\begin{cases} f_\alpha^{eq}(\mathbf{r},t)=\rho\omega_\alpha\Big[1+3(\mathbf{e}_\alpha\cdot\mathbf{u})+\dfrac{9}{2}(\mathbf{e}_\alpha\cdot\mathbf{u})^2-\dfrac{3}{2}|\mathbf{u}|^2\Big], \\ g_\alpha^{eq}(\mathbf{r},t)=T\omega_\alpha\Big[1+3(\mathbf{e}_\alpha\cdot\mathbf{u})+\dfrac{9}{2}(\mathbf{e}_\alpha\cdot\mathbf{u})^2-\dfrac{3}{2}|\mathbf{u}|^2\Big], \end{cases} \tag{2.3}$$

where $\mathbf{r}$ is the space position vector, δ_t is the discrete time step. The values of the weights are: $\omega_0=2/9$, $\omega_\alpha=1/9$ for $\alpha=1\sim 6$ and $\omega_\alpha=1/72$ for $\alpha=7\sim 14$, $\mathbf{u}$ denotes the macro fluid velocity at each lattice node which can be calculated by $\mathbf{u}=(\sum_{\alpha=0}^{14} f_\alpha e_\alpha+\frac{1}{2}\mathbf{F}_B\delta_t)/\rho$, the macro fluid density is $\rho=\sum_{\alpha=0}^{14} f_\alpha$ and the macro temperature can be calculated by

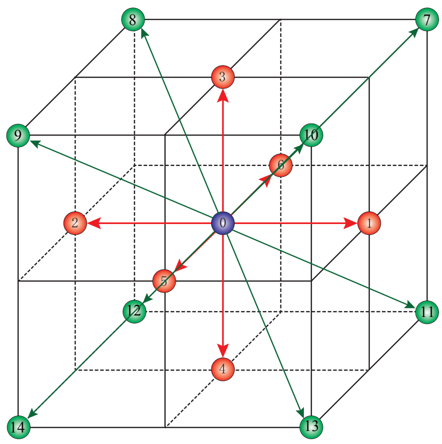

Figure 1: Diagram of the D3Q15 model.

$T=\sum_{\alpha=0}^{14} g_\alpha+\frac{1}{2}Q_B\delta_t$. t denotes time, τ_f and τ_g denote the non-dimensional relaxation times of the density and temperature evolutions, respectively, which can be expressed as

$$\left\{\begin{aligned}\tau_f&=\frac{L_c u_0}{Rec_s^2\delta_t}+0.5,\\ \tau_g&=\frac{L_c u_0}{RePrc_s^2\delta_t}+0.5,\end{aligned}\right. \tag{2.4}$$

where c_s is the lattice speed of sound, L_c and u_0 are the characteristic length and velocity, respectively and $Re=\rho u_0 L_c/\mu$ and $Pr=c_p\mu/\kappa$ are the Reynolds and Prandtl numbers, respectively. F_α and G_α in Eq. (2.1) are the source terms which are evaluated via the IBM in Section 2.2.

2.2 Immersed boundary method

In this study, the momentum exchange-based IBM proposed by Niu et al. [24] is adopted to treat the boundary conditions on the particle surface. Firstly, we introduce an important tool, the discrete Delta function [25]

$$D_{ijk}(\mathbf{r}_{ijk}-\mathbf{X}_l)=\frac{1}{h^3}\delta_h\left(\frac{x_{ijk}-X}{h}\right)\delta_h\left(\frac{y_{ijk}-Y}{h}\right)\delta_h\left(\frac{z_{ijk}-Z}{h}\right), \tag{2.5}$$

where $\mathbf{X}_l(X,Y,Z)$ is the solid coordinate, the subscript l denotes those variables at the location of the solid particles, $\sum_l$ stands for a loop on all the Lagrangian points on the particle surface, h is the LBM mesh spacing and

$$\delta_h(a)=\left\{\begin{array}{ll}\frac{1}{4}\Big(1+\cos\Big(\frac{\pi|a|}{2}\Big)\Big), & \text{when } |a|\le 2,\\ 0, & \text{otherwise.}\end{array}\right. \tag{2.6}$$

Using Eqs. (2.5) and (2.6), the fluid macro variables at the solid locations can be numerically obtained. Meanwhile, the effect of solid movement and temperature difference on the fluid flow can be also considered. For example, the fluid velocity and temperature on the solid particles are evaluated using the numerical interpolation from the circumambient fluid points as below

$$\left\{\begin{aligned}\mathbf{u}_f(\mathbf{X}_l,t)&=\sum_{ijk}\mathbf{u}_f(\mathbf{r},t)D_{ijk}(\mathbf{r}_{ijk}-\mathbf{X}_l)h^3,\\ T_f(\mathbf{X}_l,t)&=\sum_{ijk}T_f(\mathbf{r},t)D_{ijk}(\mathbf{r}_{ijk}-\mathbf{X}_l)h^3.\end{aligned}\right. \tag{2.7}$$

Then, these density and temperature distribution functions are modified by the local particle velocity and heat transfer between the two phases with different temperatures, respectively. Based on the momentum exchange rule, the source terms F_α and G_α in Eq. (2.1) can be calculated now as

$$\begin{cases} F_\alpha=\left(1-\dfrac{1}{2\tau_f}\right)\omega_\alpha\left(3\dfrac{\mathbf{e}_\alpha-\mathbf{u}}{c^2}+9\dfrac{\mathbf{e}_\alpha\cdot\mathbf{u}}{c^4}e_\alpha\right)\cdot\mathbf{F}_B(\mathbf{r},t), & \text{for velocity } BC,\\ \quad\text{where } \mathbf{F}_B(\mathbf{r},t)=\sum\limits_l\mathbf{F}_f(\mathbf{X}_l,t)D_{ijk}(\mathbf{r}_{ijk}-\mathbf{X}_l)\Delta s_l, & \\ \quad\text{where } \mathbf{F}_f(\mathbf{X}_l,t)=2\rho(\mathbf{X}_l,t)(\mathbf{u}_s(\mathbf{X}_l,t)-\mathbf{u}_f(\mathbf{X}_l,t))h/\delta t, & \\ G_\alpha=\left(1-\dfrac{1}{2\tau_g}\right)\omega_\alpha Q_B(\mathbf{r},t), & \text{for thermal } BC,\\ \quad\text{where } Q_B(\mathbf{r},t)=\sum\limits_l Q(\mathbf{X}_l,t)D_{ijk}(\mathbf{r}_{ijk}-\mathbf{X}_l)\Delta s_l, & \\ \quad\text{where } Q(\mathbf{X}_l,t)=2(T_s(\mathbf{X}_l,t)-T_f(\mathbf{X}_l,t))h/\delta_t, & \end{cases} \tag{2.8}$$

where Δs_l is the area that each Lagrangian point occupies on the particle surface.

2.3 Evaluation of the drag coefficient and average Nusselt number

In the multi-phase coupling simulation, the transferred terms such as the interaction forces and heat flux on an isolated particle are evaluated by Eq. (2.9) where $\mathbf{f}_d$ is the drag force, A is the front area, ρ is the fluid density, u_0 is the uniform inlet field velocity far from the particle, q is the heat flux, h_e is the convective heat transfer coefficient of the fluid, S is the surface area, κ is the thermal conductivity coefficient of the fluid, D is the the volume-equivalent sphere diameter and T_s and T_f are the temperature of the solid and fluid, respectively.

$$\begin{cases} \mathbf{f}_d=\dfrac{1}{2}CdA\rho u_0^2,\\ q=h_eS(T_s-T_f),\\ Nu=h_eD/\kappa. \end{cases} \tag{2.9}$$

Note that Nu should be obtained prior to the calculation of q since h_e is unknown. In the particle scale numerical simulation, the average Nusselt number is calculated as [29]

$$Nu=\frac{\sum\limits_l Q(\mathbf{X}_l,t)\Delta s_l}{\kappa S(T_h-T_c)}D, \tag{2.10}$$

where T_h and T_c denote the high and low temperature in the system, respectively. Cd can be calculated as soon as $\mathbf{f}_d$ is obtained which is calculated as

$$\mathbf{f}_d=\mathbf{f}_x=-\sum_l F_x(\mathbf{X}_l,t)\Delta s_l, \tag{2.11}$$

where F_x is the one component of $\mathbf{F}_f$ in X-directions.

3 Computational issues

In this study, we conduct numerical simulations in a rectangular duct containing two equally sized hot particles. The inter particle distance between two particles centers is L as shown in Fig. 2. In a Cartesian coordinate system, the solid particle can be well defined as follows

$$\frac{x^2}{\breve{a}^2}+\frac{y^2}{\breve{b}^2}+\frac{z^2}{\breve{c}^2}=1, \tag{3.1}$$

where the parameters $\breve{a}$, $\breve{b}$ and $\breve{c}$ are the principal semi-axes along X direction, Y direction and Z direction, respectively. The aspect ratio is defined as $Ar=\breve{a}/\breve{b}$ or $Ar=\breve{a}/\breve{c}$ since $\breve{b}=\breve{c}$ in this study. Fig. 2 gives a brief sketch map in which the computational domain is $20D\times 10D\times 10D$. The size of the computational domain has been tested and used in our previous study [13] and those from others like Gilmanov et al. [6], Zastawny et al. [46], Rong et al. [32] and Guan et al. [7]. Furthermore, for the IBM, it requires special treatment and caution in the generation of Lagrangian points on the particle surface. In this work, the mesh generation on particle surface is performed following two steps. Firstly, we set $Ratio=1.0$ ($Ratio=d_s/h^2$, d_s is the area of each triangular element, h is the grid space) and the CVDT grids are formed on the surface of a unit sphere with approximately equal size. Secondly, the Lagrangian points on the surface of a spherical particle are mapped into an ellipsoid by topological transformation. The advantage of this treatment is that the unit sphere grid can be called many times for generating multiple particles with different sizes, spatial distributions and velocities.

We use a mesh system of $512\times 256\times 256$ to conduct all the simulations which is also picked through a set of case studies [13]. In our previous work [13], the grid independence study was carried out for the case of flow past an isolated sphere, good convergence was observed for the normalized drag coefficient and average Nusselt number

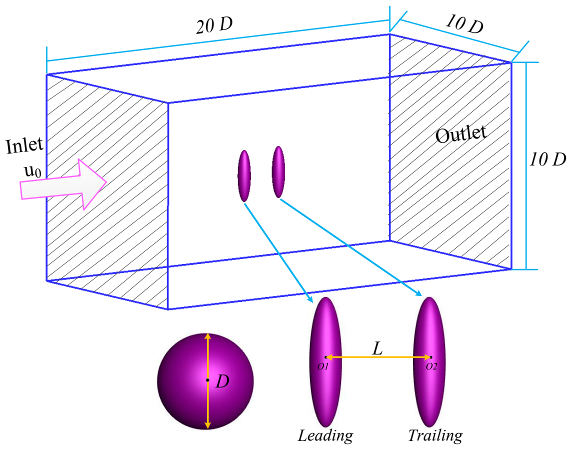

Figure 2: The computational domain for flow past two hot stationary spherical particles.

Table 1: Specifications of our test platform.

Operating System	CentOS 7.3
CPU Type	Intel(R) Xeon(R) CPU E5-2620 v4
CPU Clock	2.10GHz $\times$ 32 cores
Host Memory Size	96GB
GPU Type	NVIDIA Tesla K40C
GPU Clock	3.0 GHz $\times$ 2880 cores
Device Memory Size	12.0 GB
Host Compiler	g++ (GCC) 4.8.5
Device Compiler	nvcc 8.0

at different Reynolds numbers under the current grid scale. The characteristic velocity $u_0 = 0.05$ and the velocities of the four solid boundary are also set as u_0. The temperature is normalized by

$$\tilde{T} = (T - T_c)/(T_h - T_c)$$

in the non-dimensional calculations, T_f is inlet and initial temperature of fluid, which is equal to the minimum temperature T_c, T_s represents the constant particle temperature which is equal to the maximum temperature T_h, therefore, $\tilde{T}_s = 1$ and $\tilde{T}_f = 0$ are the dimensionless forms for particle and fluid, respectively. For non-spherical particles, the characteristic length is $L_c = D$ and $Pr = 0.744$.

At last, in this paper, the in-house code is implemented based on the CPU-GPU heterogeneous architecture [13, 44]. In the CPU-GPU heterogeneous computer system, the GPU cooperates with the CPU in the complicated calculation progress, Table 1 lists the specifications of our platform.

There are five major steps in the IB-LBM calculation: (1) Initialization, (2) Streaming step and boundary processing, (3) Fluid-solid interaction with IBM, (4) Collision step, (5) Checking convergence and saving results. In the first procedure, the fluid particle distribution functions and the corresponding moments are initialized according to the velocity, temperature, Reynolds number and Prandtl numbers. This information is sent from the host to the device. This procedure is carried out only once and thus performed based on serial processing. For the second procedure, the fluid particles stream along the fifteen velocity directions and the new distribution function vectors $f_\alpha(\mathbf{r},t)$ and $g_\alpha(\mathbf{r},t)$ will be obtained with consideration of the boundary conditions. For the third procedure, fluid-solid interaction is implemented based on IBM and the force and heat transfer between fluid and solid are computed. For the fourth procedure, the collision distribution function vectors will be calculated in the collision function which is a local operation. Procedures (2)-(4) will be repeatedly performed which take most of the computing time. Therefore, these calculations are fully parallelized. The last procedure, checking convergence and saving results, is also required to be done frequently. However, the checking frequency is much lower than the main calculation in procedures (2)-(4) (in our code, it was checked every 1000 iterations), so this part is not parallelized.

4 Validation case

Though the current IB-LBM code has been validated in our previous study [13] on a fixed hot sphere, two validation cases are presented below to remove the doubt on its capability to treat two interactive particles and also to make this paper self-contained.

4.1 Cold flow over an isolated hot sphere

In the first validation case, we only consider one hot sphere in the calculation. The Reynolds numbers are varied from 20 to 200 and the Prandtl number is set as either $Pr=0.744$ or $Pr=1.0$. The currently obtained results are compared with the numerical results of Tavassoli et al. [37] and the predicted results from the empirical formulas provided by Ranz [28], Feng and Michaelides [5] and Richter and Nikrityuk [30], respectively. These formulas are given in Table 2.

Table 2: The empirical formulas of average Nusselt number.

References	Formulas	Limits
Ranz [28]	Nu=2.0+0.6$Re^{0.5}Pr^{0.33}$	$10<Re<10^4$, $Pr>0.7$
Feng and Michaelides [5]	Nu=2.0+$(0.4Re^{0.5}+0.06Re^{2/3})Pr^{0.4}$	$3.5<Re<7.6\times10^4$, $0.7<Pr<380$
Richter and Nikrityuk [30]	Nu=1.76+0.55$Re^{0.5}Pr^{1/3}$+0.014$Pr^{1/3}Re^{2/3}$	$10<Re<250$, $Pr>0.7$

Results for the average Nusselt numbers plotted over the Reynolds numbers are shown in Fig. 3. It can be seen that when $Pr=0.744$ (Fig. 3(a)) the results obtained in the current study are well in alignment with the correlations by Ranz [28] and Feng and Michaelides [5]. Other correlations result in slightly lower values. Similar phenomenon can be also found in Fig. 3(b) when $Pr=1.0$. Particularly, the current numerical results agree very well with the simulation results from Tavassoli et al. [37]. Therefore, it is reasonable to conclude that the current IB-LBM model can produce accurate results for forced convection problems involving one sphere.

4.2 Flow past two interacting spheres

To further analyze the behavior of a forced flow around a pair of spheres, a setup with two spheres of tandem arrangement is considered as shown in Fig. 2 (when $\breve{a}=\breve{b}=\breve{c}$). We consider six inter particle distances $(L/D=1.5,2,3,4,6,8)$ and three Reynolds numbers $(Re=30,61,100)$ to construct different circumstance. Then, the results are compared with the results of Zhu et al. [48], Tsuji et al. [39] and Rong at al. [32]. In this subsection and following ones, the drag ratio is defined as Cd_i/Cd_0 $(i=1,2)$, where Cd_1 is the drag coefficient of the leading particle, Cd_2 is the drag coefficient of the trailing particle and Cd_0 is the drag coefficient of a single non-interacting particle. The ratio of the average Nusselt number Nu_i/Nu_0 is defined in a similar way.

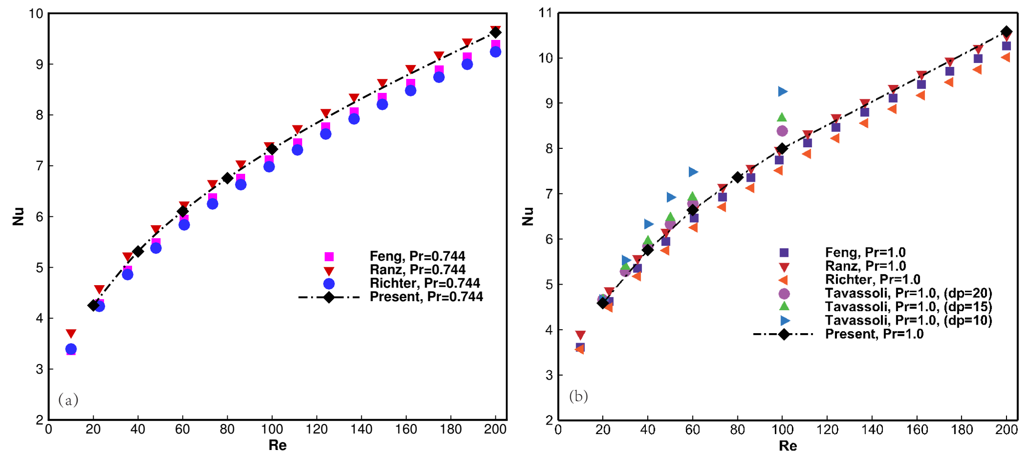

Figure 3: Average Nusselt number versus Reynolds number for the forced convection over a fixed hot sphere. (a) $Pr=0.744$ and (b) $Pr=1.0$.

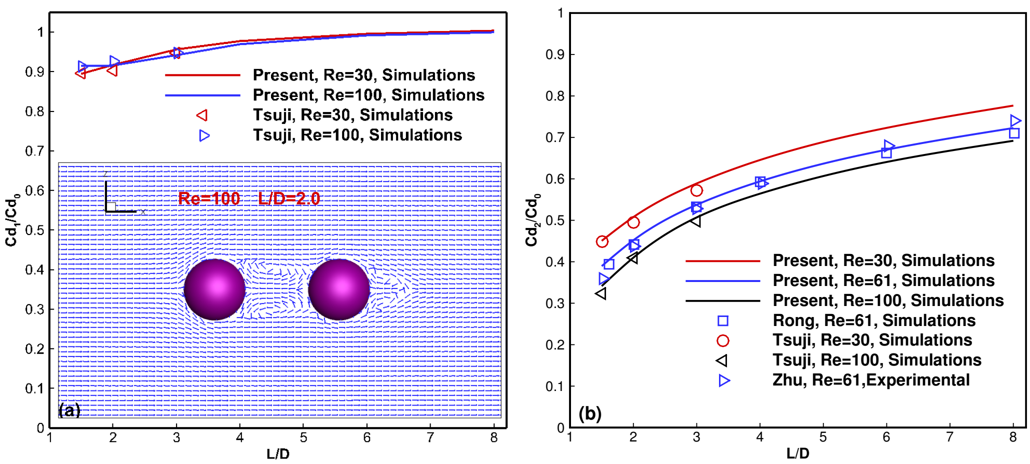

Figure 4: Drag ratio of two tandem particles, (a) for the leading particle and (b) for the trailing particle.

Fig. 4 shows the drag ratios between the two particles changing with the inter particle distance at three different Reynolds numbers. From Fig. 4(a), we find that the change in Cd_1/Cd_0 is very small (less than 10%), this trend is qualitatively in line with the observations of Tsuji et al. [39] and the same trend is observed at other Reynolds numbers. Note that there is no available experimental data at $Re=30$ and $Re=100$, the inset figure in Fig. 4(a) is the simulated flow field when $Re=100$ and $L/D=2.0$. Fig. 4(b) shows that Cd_2/Cd_0 increases with the inter particle distance L indicating a decline of the influence of the leading particle. Similar experimental results were also reported by Zhu et al. [48] at $Re=61$ and other results generated by numerical simulations (Tsuji et al. [39] and Rong at al. [32]). Above two steps of validation also show that the computational domain and grid scale in the present work are reasonable.

5 Results and discussions

In this section, we conduct computations for thermal flows past two tandem spheroids as schematically shown in Fig. 2. In order to investigate the combined effects of the aspect ratio $(Ar=1.0,1.5,2.0,2.5,4.0)$, inter particle distance $(L=1.5D,2.0D,3.0D,5.0D,7.0D)$ and Reynolds numbers ($Re=10,25,50,100,200$), totally, 125 numerical cases are carried out.

The distribution of the non-dimensional fluid temperature together with the streamlines around the two spheroids in the X-Z plane at $Y=5D$ are shown in Fig. 5. For the sake of clarification, only the cases when $Re=100$, $Ar=1.0,4.0$ and $L=1.5D,7.0D$ are presented as typical examples. From Figs. 5(a)-(d), it can be seen that flow separation behind both the two particles takes place for both the values of Ar and L. Due to the reduce of the frontal area and thus the resistance to the fluid flow, the length of the recirculation wake for $Ar=1.0$ is shorter than $Ar=4.0$. Furthermore, when comparing Figs. 5(a) and (b) (or Figs. 5(c) and (d)) for the same Ar, the recirculation wake of the leading particle is further distributed by with the trailing particle when $L=1.5D$ whereas does not reach the trailing particle for both $Ar=1.0,4.0$ when $L=7.0D$. This phenomenon shows that the inter particle distance L plays a key role in the interaction between the two particles in a tandem arrangement. Meanwhile, it is also shown that, regardless of L, the length of the recirculation wake behind the trailing particle is much shorter as compared to that of an isolated one due to less shear experienced by the trailing particle. Therefore, it is concluded that for a given Ar, with the increase of L, the recirculation wake behind the leading particle also increases reflecting that the particle-particle interactions decrease with the increase of L.

5.1 Drag coefficient

Fig. 6 shows the drag coefficients of the two particles at different Re, Ar and L, quantitatively. It can be seen that both Cd_1 and Cd_2 are seriously influenced by these key

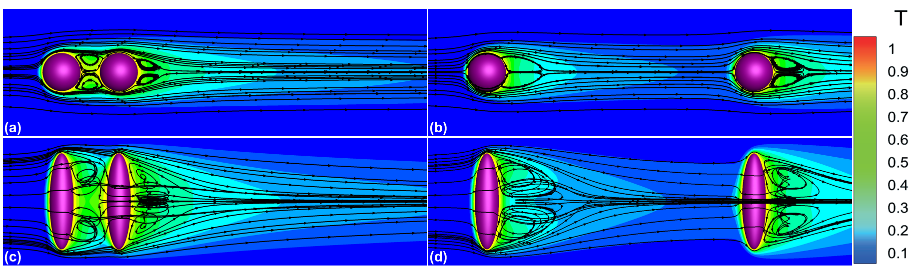

Figure 5: Temperature distributions and streamlines at $Re=100$ in different cases ((a): $Ar=1.0$, $L=1.5D$; (b): $Ar=1.0$, $L=7.0D$; (c): $Ar=4.0$, $L=1.5D$; (d): $Ar=4.0$, $L=7.0D$).

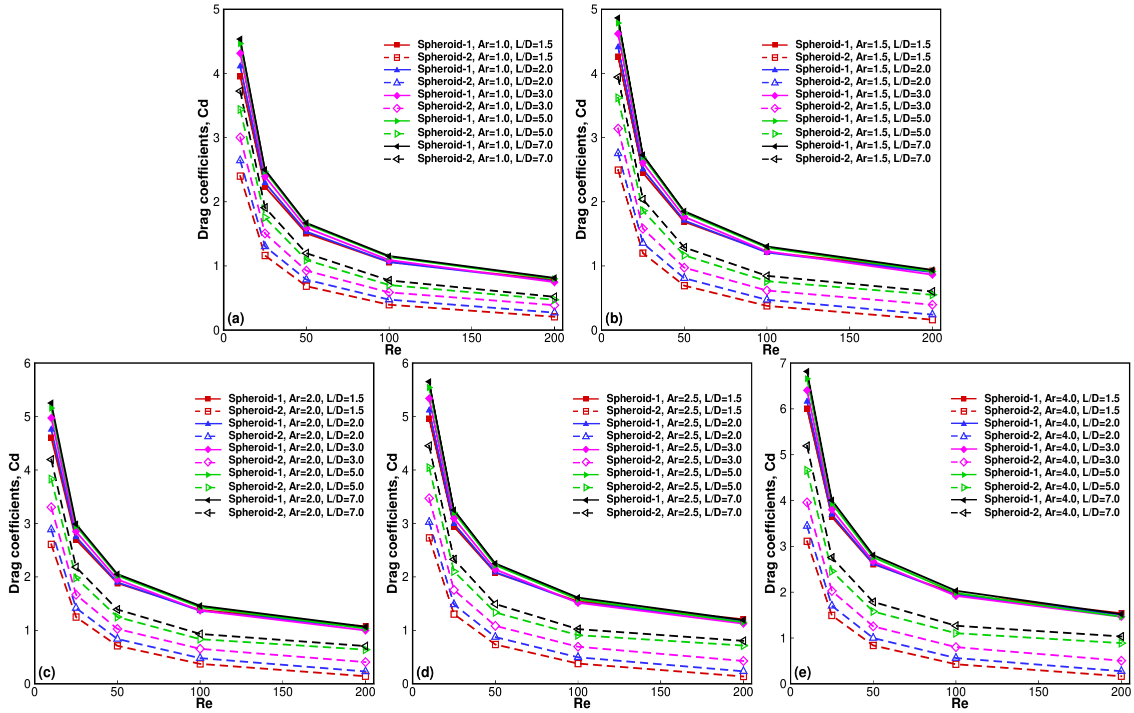

Figure 6: Effects of Re and L on the drag coefficients Cd of two tandem spheroid particles with different aspect ratio Ar.

parameters. Regardless of the shape factor described by the aspect ratio Ar and particle-particle interactions described by the inter particle distance L, the characteristic of the drag coefficients versus Re is clearly observed, that is, both Cd_1 and Cd_2 decrease with Re. This phenomenon is in line with results on a single hot spheroid immersed in a cold fluid. It is also found that irrespective of Re and L, both Cd_1 and Cd_2 increase with Ar. For a given Ar at the same Re, both Cd_1 and Cd_2 increase with L. Again, this is consistent with existing experimental studies for the case of two tandem spheres ($Ar=1$) [2]. Figs. 6(a)-(e) also shows that the influence of the geometry factors on the trailing particle is much larger than that on the leading one. For given Reynolds number Re, aspect ratio Ar and inter particle distance L, Cd_1 is very close to that of an isolated one immersed in a fluid. On the contrary, Cd_2 is far less than Cd_0 [13]. With the decrease of L, the difference between Cd_2 and Cd_0 becomes larger, especially when $Re=200$. Taking the aspect ratio $Ar=2.0$ as an example (shown as Fig. 6(c)), the corresponding data is attached in Table 3.

Fig. 7 shows the ratio between the drag coefficients of the trailing and leading particles (Cd_2/Cd_1) at different Re, Ar and L. It is clearly shown that Cd_1 is always larger than Cd_2 because of the reduced stresses acting on the trailing particle. This trend was also reported by the experimental and numerical results [26,48] for two tandem spheres and

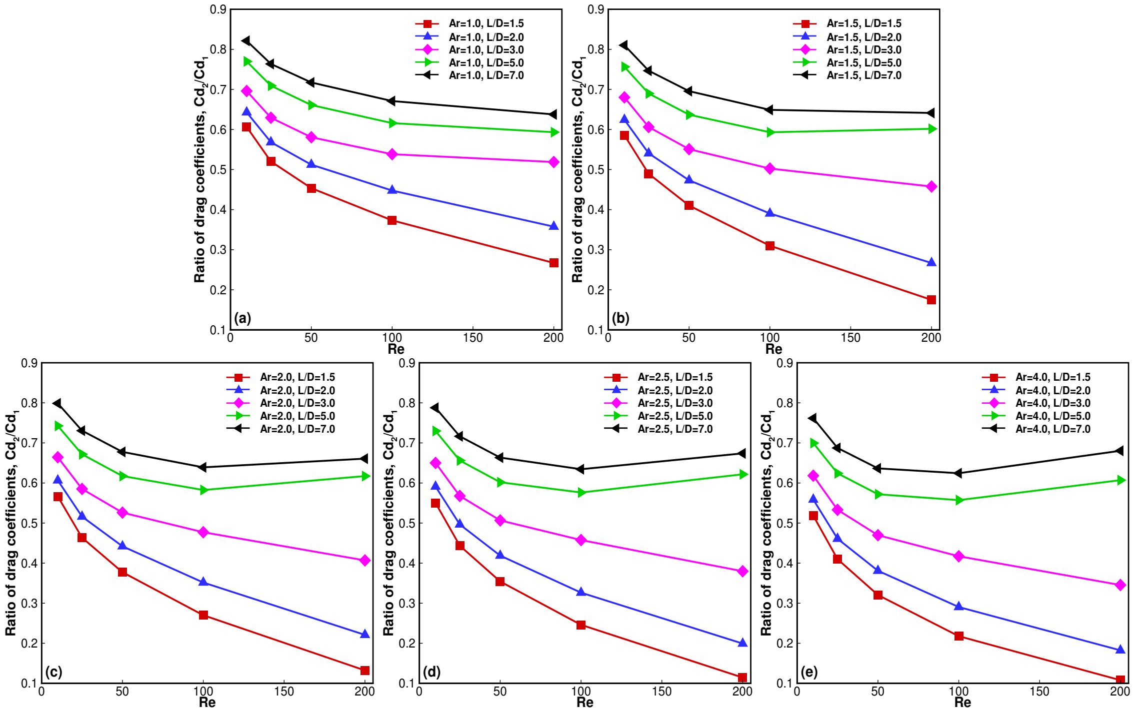

Figure 7: Effects of Re and L on the ratio of drag coefficients Cd_2/Cd_1 of two tandem spheroid particles with different aspect ratio Ar.

non-spherical particles in the 2D situation [16]. Moreover, for two tandem spheroids, Cd_2/Cd_1 decreases when lifting the Reynolds number. However, when $Re>100$ with aspect ratio $Ar=2.0,2.5,4.0$ and inter particle distance $L/D=5.0,7.0$, Cd_2/Cd_1 increases with Re. This is because the influence of the leading particle on the trailing one is reduced when Re and L increase. For all the considered Ar, Cd_2/Cd_1 decreases when lifting Re and increases with L. At last, for a given inter particle distance L, Cd_2/Cd_1 decreases with the increase of the aspect ratio Ar regardless of Re. As the inter particle distance L increases, the drag coefficients of both the two particles increase meanwhile Cd_2/Cd_1 also increases. As a fact, from Figs. 7(a)-(e), it is found that Cd_2/Cd_1 is always less than

Table 3: Comparison of individual drag coefficient of two tandem spheroids to the drag coefficient of a single spheroid at aspect ratio $Ar=2.0$.

Re	$L/D=1.5$		$L/D=2.0$		$L/D=3.0$		$L/D=5.0$		$L/D=7.0$	
	Cd_1/Cd_0	Cd_2/Cd_0	Cd_1/Cd_0	Cd_2/Cd_0	Cd_1/Cd_0	Cd_2/Cd_0	Cd_1/Cd_0	Cd_2/Cd_0	Cd_1/Cd_0	Cd_2/Cd_0
10	0.884	0.500	0.913	0.554	0.954	0.634	0.990	0.735	1.000	0.805
25	0.902	0.418	0.920	0.475	0.954	0.558	0.988	0.664	1.000	0.731
50	0.916	0.346	0.923	0.408	0.949	0.499	0.984	0.608	0.998	0.676
100	0.942	0.254	0.931	0.327	0.935	0.446	0.977	0.569	0.994	0.635
200	0.993	0.131	0.967	0.214	0.924	0.376	0.957	0.591	0.988	0.653

Table 4: Comparison of average total drag coefficient of two tandem spheroids to the total drag coefficient of a single spheroid at various simulation parameters.

Re	$Ar=1.0$		$Ar=1.5$		$Ar=2.0$		$Ar=2.5$		$Ar=4.0$	
	Cd_{avg}	Cd_{avg}/Cd_0	Cd_{avg}	Cd_{avg}/Cd_0	Cd_{avg}	Cd_{avg}/Cd_0	Cd_{avg}	Cd_{avg}/Cd_0	Cd_{avg}	Cd_{avg}/Cd_0
	$L=1.5D$									
10	3.179	0.705	3.376	0.699	3.607	0.692	3.846	0.687	4.554	0.676
25	1.697	0.679	1.825	0.669	1.971	0.660	2.122	0.654	2.567	0.642
50	1.096	0.655	1.190	0.641	1.297	0.631	1.407	0.623	1.726	0.612
100	0.727	0.628	0.798	0.609	0.878	0.598	0.960	0.591	1.194	0.583
200	0.492	0.601	0.545	0.576	0.608	0.562	0.672	0.556	0.853	0.552
	$L=2.0D$									
10	3.378	0.749	3.582	0.741	3.821	0.733	4.070	0.726	4.801	0.713
25	1.799	0.720	1.931	0.708	2.082	0.698	2.239	0.690	2.698	0.675
50	1.160	0.693	1.258	0.678	1.369	0.665	1.482	0.656	1.811	0.643
100	0.768	0.663	0.841	0.642	0.924	0.629	1.009	0.622	1.251	0.611
200	0.516	0.630	0.572	0.604	0.639	0.590	0.706	0.584	0.894	0.578
	$L=3.0D$									
10	3.658	0.812	3.879	0.803	4.138	0.794	4.404	0.786	5.181	0.769
25	1.949	0.780	2.093	0.768	2.257	0.756	2.426	0.747	2.914	0.729
50	1.260	0.753	1.369	0.738	1.490	0.724	1.612	0.714	1.963	0.697
100	0.839	0.724	0.922	0.704	1.013	0.690	1.105	0.681	1.360	0.665
200	0.568	0.693	0.629	0.665	0.702	0.650	0.777	0.643	0.984	0.636
	$L=5.0D$									
10	3.952	0.877	4.203	0.870	4.494	0.862	4.793	0.856	5.658	0.840
25	2.113	0.846	2.278	0.836	2.464	0.826	2.653	0.817	3.196	0.800
50	1.372	0.820	1.498	0.807	1.637	0.796	1.776	0.787	2.170	0.770
100	0.921	0.795	1.023	0.781	1.135	0.773	1.245	0.767	1.543	0.754
200	0.636	0.777	0.732	0.773	0.837	0.774	0.934	0.772	1.176	0.761
	$L=7.0D$									
10	4.130	0.916	4.404	0.911	4.723	0.906	5.051	0.902	6.004	0.891
25	2.204	0.882	2.383	0.874	2.585	0.866	2.790	0.859	3.380	0.846
50	1.434	0.857	1.571	0.846	1.721	0.837	1.872	0.829	2.298	0.816
100	0.964	0.832	1.074	0.820	1.197	0.815	1.318	0.812	1.649	0.806
200	0.666	0.813	0.769	0.813	0.887	0.820	0.998	0.826	1.277	0.826

1, that is to say, the individual drag coefficient of leading particle is always greater than that of the trailing one at the same working condition. The inter particle distance L has a greater influence on the trailing particle than the leading one. When $L/D=1.5$, Cd_2/Cd_1 decreases fastest with the increase of the Reynolds number Re for all the aspect ratios Ar. The sharp decrease is caused by the strong effect of the wake structure of the leading particle on the trailing one when they are close to each other.

The average drag coefficient ($Cd_{avg}=0.5[Cd_1+Cd_2]$) of the two tandem spheroids is compared to the drag coefficient of an isolated spheroid (Cd_0) in Table 4. For a given inter particle distance L, the average drag coefficient Cd_{avg} increases with the decrease of Re but with the increase of Ar. For a fixed Reynolds number Re, Cd_{avg}/Cd_0 decreases with the increase of Ar. But under the condition of $Re=200$ and $L/D=7.0$, Cd_{avg}/Cd_0 slightly increases. This is probably because the interaction between the two particles is weakened at a large Ar. For given Re and Ar, Cd_{avg}/Cd_0 increases with L indicating that the average drag coefficient on two tandem spheroids is approaching to and that on an isolated spheroid.

Table 4 also reflects that when $L/D=7.0$, regardless of Re and Ar, the values of Cd_{avg}/Cd_0 are all greater than 0.8 which are very close or even greater than 0.9 at $Re=10$. Yet, Cd_{avg}/Cd_0 are between 0.552 to 0.705 when $L/D=1.5$. In addition, the average range of fluctuation is about 11%. When $L/D\leq 3.0$, the fluctuations of Cd_{avg}/Cd_0 are all more than 10%. When $L/D\geq 5.0$, the fluctuations of Cd_{avg}/Cd_0 are all less than 10% except for the cases of aspect ratio $Ar=1.0$. These phenomenons show that particle shape and relative distance have great influences on the flow structure and force evolution.

5.2 Average Nusselt number

Fig. 8 shows the average Nusselt numbers at various Reynolds number Re, aspect ratio Ar and inter particle distance L, quantitatively. Similar to the drag coefficient, those average Nusselt numbers are also seriously influenced by these key parameters. On the one hand, regardless of Ar and L, both Nu_1 and Nu_2 increase with Re. On the other hand, irrespective of the Reynolds number Re and inter particle distance L, both Nu_1 and Nu_2 increase with Ar. For given Ar and Re, both Nu_1 and Nu_2 increase with L. Further anal-

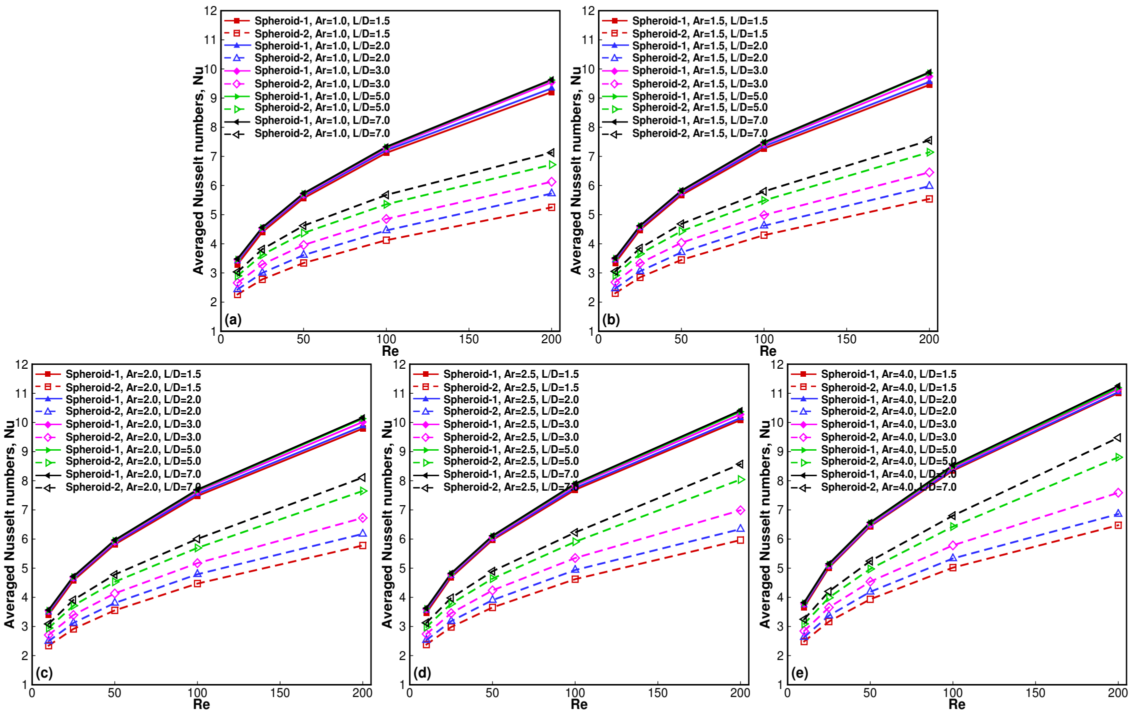

Figure 8: Effects of Re and L on the average Nusselt number Nu of two tandem spheroid particles with different aspect ratio Ar.

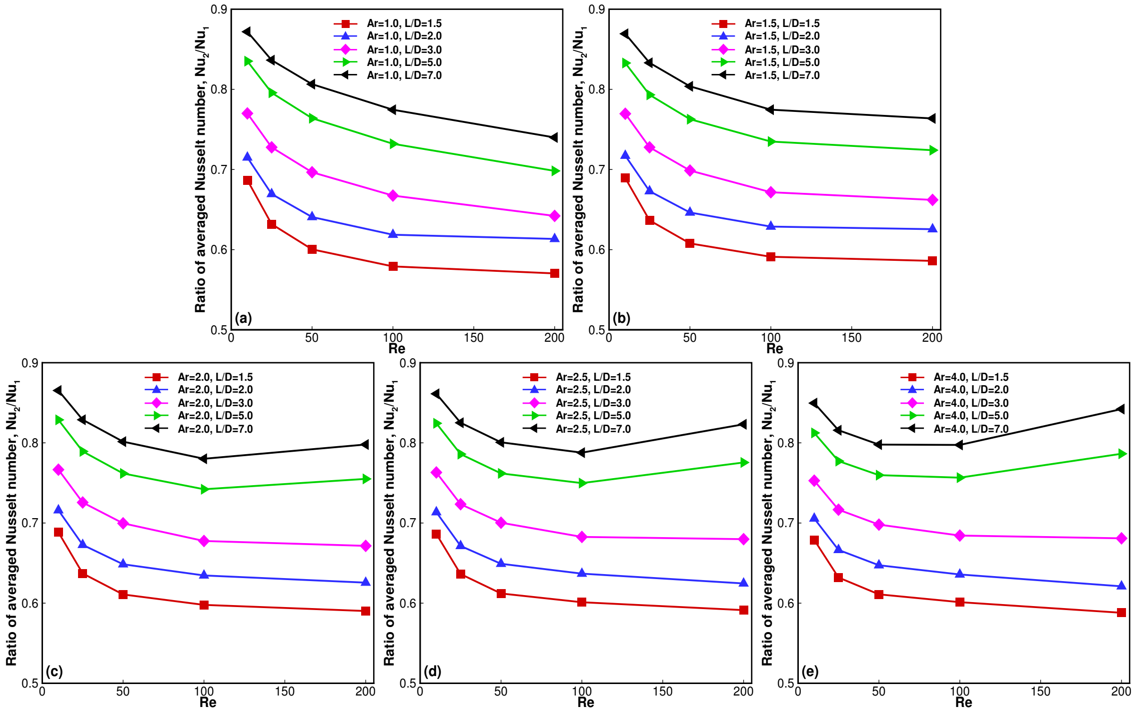

Figure 9: Effects of Re and L on the ratio of average Nusselt Number Nu_1/Nu_2 of two tandem spheroid particles with different aspect ratio Ar.

ysis on Fig. 8 shows that both Nu_1 and Nu_2 are increasing with the increase of Reynolds number Re at the same aspect ratio and inter particle distance. The variation range of Nu_2 is larger than Nu_1 and Nu_1 and Nu_0 are almost equal. In addition, the change of $Nu_0 - Nu_2$ for the trailing particle is much similar to it's drag coefficient, especially at Reynolds number $Re=10$ and the corresponding data can be found in Table 5. The trend of the Nu distribution is consistent with the drag coefficients because the heat transfer characteristic is highly determined by the fluid flow field.

Fig. 9 shows the combined effect of Re and L on Nu_2/Nu_1. It is not surprising to find that all the ratios are below 1 and most of them decrease with the increase of Re.

Table 5: Comparison of individual averaged Nusselt number of two tandem spheroids to the averaged Nusselt number of a single spheroid at aspect ratio $Ar=2.0$.

Re	$L/D=1.5$		$L/D=2.0$		$L/D=3.0$		$L/D=5.0$		$L/D=7.0$	
	Nu_1/Nu_0	Nu_2/Nu_0	Nu_1/Nu_0	Nu_2/Nu_0	Nu_1/Nu_0	Nu_2/Nu_0	Nu_1/Nu_0	Nu_2/Nu_0	Nu_1/Nu_0	Nu_2/Nu_0
10	0.955	0.658	0.979	0.701	0.992	0.760	0.998	0.827	1.000	0.867
25	0.970	0.618	0.983	0.661	0.991	0.719	0.998	0.788	1.000	0.829
50	0.975	0.595	0.984	0.638	0.990	0.693	0.997	0.759	1.000	0.801
100	0.971	0.580	0.980	0.622	0.991	0.671	0.996	0.739	0.999	0.779
200	0.962	0.568	0.970	0.607	0.984	0.661	0.995	0.751	0.998	0.797

Table 6: Comparison of Nu_{avg} and Nu_0 at various simulation parameters.

Re	$Ar=1.0$		$Ar=1.5$		$Ar=2.0$		$Ar=2.5$		$Ar=4.0$	
	Nu_{avg}	Nu_{avg}/Nu_0	Nu_{avg}	Nu_{avg}/Nu_0	Nu_{avg}	Nu_{avg}/Nu_0	Nu_{avg}	Nu_{avg}/Nu_0	Nu_{avg}	Nu_{avg}/Nu_0
	$L=1.5D$									
10	2.780	0.799	2.824	0.805	2.873	0.806	2.923	0.807	3.071	0.806
25	3.590	0.787	3.663	0.793	3.747	0.794	3.833	0.795	4.093	0.795
50	4.455	0.777	4.559	0.782	4.684	0.785	4.810	0.787	5.185	0.788
100	5.622	0.766	5.783	0.772	5.975	0.776	6.157	0.778	6.684	0.783
200	7.229	0.750	7.496	0.757	7.784	0.765	8.025	0.769	8.741	0.775
	$L=2.0D$									
10	2.919	0.839	2.951	0.841	2.993	0.840	3.039	0.839	3.183	0.835
25	3.744	0.821	3.803	0.823	3.879	0.822	3.962	0.822	4.217	0.819
50	4.628	0.807	4.719	0.810	4.837	0.811	4.959	0.811	5.330	0.811
100	5.833	0.795	5.984	0.799	6.171	0.801	6.345	0.802	6.861	0.803
200	7.530	0.781	7.768	0.785	8.024	0.788	8.248	0.791	8.950	0.793
	$L=3.0D$									
10	3.057	0.879	3.082	0.878	3.122	0.876	3.167	0.874	3.310	0.868
25	3.910	0.857	3.960	0.857	4.035	0.855	4.117	0.854	4.374	0.849
50	4.823	0.841	4.905	0.842	5.021	0.841	5.145	0.841	5.521	0.840
100	6.061	0.826	6.207	0.829	6.403	0.831	6.591	0.833	7.116	0.833
200	7.836	0.813	8.097	0.818	8.371	0.822	8.632	0.828	9.367	0.830
	$L=5.0D$									
10	3.187	0.916	3.211	0.915	3.252	0.913	3.299	0.910	3.448	0.904
25	4.087	0.896	4.135	0.895	4.211	0.893	4.295	0.891	4.561	0.886
50	5.046	0.880	5.123	0.879	5.240	0.878	5.368	0.878	5.761	0.876
100	6.335	0.864	6.478	0.865	6.686	0.868	6.892	0.871	7.462	0.874
200	8.167	0.847	8.503	0.859	8.891	0.873	9.206	0.883	10.002	0.887
	$L=7.0D$									
10	3.259	0.937	3.285	0.936	3.328	0.934	3.377	0.932	3.535	0.927
25	4.188	0.918	4.237	0.917	4.315	0.915	4.402	0.913	4.678	0.908
50	5.178	0.903	5.254	0.902	5.373	0.900	5.503	0.900	5.907	0.898
100	6.503	0.887	6.641	0.887	6.851	0.889	7.064	0.893	7.666	0.898
200	8.380	0.869	8.718	0.881	9.137	0.898	9.492	0.910	10.365	0.919

Exceptions take place when $Re>100$, $Ar\geq 2.0$ and $L/D\geq 5.0$ in which Nu_2/Nu_1 increases with *Re*. This is caused by the decreasing influence of the leading particle on the trailing one when elevating *Re* and *L*. Furthermore, for all the considered Ar, Nu_2/Nu_1 increases with *L* at the same *Re*, which is consistent with the trend of Cd_2/Cd_1. That is because the interaction between the particles is reduced when the inter particle distance *L* increases.

The comparison of $Nu_{avg}=0.5[Nu_1+Nu_2]$ and Nu_0 is conducted in Table 6. For a given inter particle distance *L*, as the values of Reynolds number *Re* increase, Nu_{avg} increases under the same Ar and *L*. And Nu_{avg} increases with the aspect ratio Ar at the same *Re* and *L*. In addition, for any Reynolds number *Re*, aspect ratio Ar and inter particle distance, all Nu_{avg}/Nu_0 is less than 1. This is due to the fact that the flow structure behind the leading particle affects the forces evolution between the trailing particles and the surrounding fluid, which will bring additional influence on the heat transfer. For a fixed Reynolds number *Re*, with the increase of aspect ratio Ar, the fluctuation range of Nu_{avg}/Nu_0 is around 5%, The results mentioned above show that particle shape and relative distance play important roles on the heat transfer.

5.3 Establishment of the prediction formula

According to the discussions above, it is found that the influence of the key factors (Reynolds number Re, aspect ratio Ar and inter particle distance L) on Cd and Nu is highly combined which generates much difficulty on the prediction. Therefore, we establish the prediction formula for Cd and Nu based on the numerical results. To this end, we begin with the relations for a single spheroid from our previous work [13]

$$Cd_0=\frac{\lambda_1}{Re}(Ar)^{\lambda_2}+\frac{\lambda_3}{\sqrt{Re}}(Ar)^{\lambda_4}+\lambda_5(Ar)^{\lambda_6}, \tag{5.1a}$$

$$Nu_0=\lambda_1 Pr^{1/3}Re^{2/3}(Ar)^{\lambda_2}+\lambda_3 Pr^{1/3}Re^{1/2}(Ar)^{\lambda_4}+\lambda_5(Ar)^{\lambda_6}. \tag{5.1b}$$

Here, these two formulas only depend on the Reynolds number Re and aspect ratio Ar. The inter particle distance L will be taken into account now. For convenience, L will be replaced by $\ell=L/D$ in the following work. In order to construct the fitting formula for spheroid-1 (leading particle), Eq. (5.1a) is extended to

$$Cd_1=\frac{P_1(\ell)}{Re}(Ar)^{c_1}+\frac{P_2(\ell)}{\sqrt{Re}}(Ar)^{c_2}+P_3(\ell)(Ar)^{c_3}, \tag{5.2}$$

where $P_i(\ell)=(a_i+b_i\ell)$, $i=1,2,3$.

Through a regression analysis on the data in Fig. 6, the unknown coefficients in Eq. (5.2) are determined as $c_1=-0.3503$, $c_2=0.6814$, $c_3=0.0863$

$$P_1(\ell)=18.7996+0.7754\ell, \tag{5.3a}$$

$$P_2(\ell)=5.3379+0.1250\ell, \tag{5.3b}$$

$$P_3(\ell)=0.3358-0.0112\ell. \tag{5.3c}$$

Quantitative comparisons between the proposed formula for Cd_1 and the numerical results are given in Fig. 10(a). It is clearly shown the formula has very good prediction capability and the average relative deviation is $\bar{\varepsilon}_{Cd_1}=1.62\%$.

Based on the same template, the fitting formula for spheroid-2 (trailing particle) is constructed as

$$Cd_2=\frac{P_1(\ell)}{Re}(Ar)^{c_1}+\frac{P_2(\ell)}{\sqrt{Re}}(Ar)^{c_2}+P_3(\ell)(Ar)^{c_3}, \tag{5.4}$$

where $P_i(\ell)=(a_i+b_i\ell^{1/3}+d_i\ell^{1/2})$, $i=1,2,3$.

The unknown coefficients in Eq. (5.4) are determined as $c_1=-0.0256$, $c_2=0.4712$, $c_3=0.7973$

$$P_1(\ell)=-29.2536+71.4374\ell^{1/3}-31.8722\ell^{1/2}, \tag{5.5a}$$

$$P_2(\ell)=8.7403-11.5953\ell^{1/3}+6.6411\ell^{1/2}, \tag{5.5b}$$

$$P_3(\ell)=-1.2898+1.9492\ell^{1/3}-0.8852\ell^{1/2}. \tag{5.5c}$$

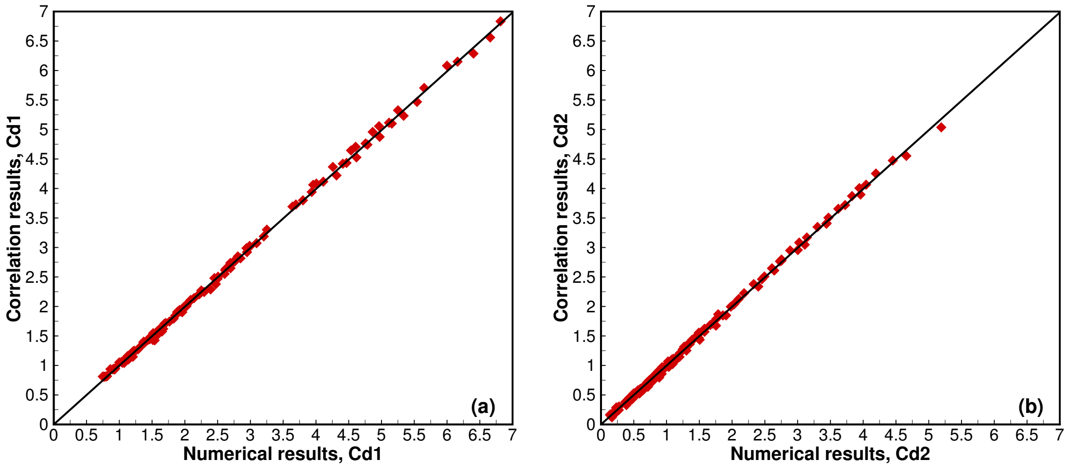

Figure 10: Parity plot of drag coefficients predicted using relations and corresponding calculations from numerical simulations. (a) Cd_1 from Eqs. (5.2) versus calculated Cd_1 and (b) Cd_2 from Eqs. (5.4) versus calculated Cd_2.

Quantitative comparisons can be found in Fig. 10(b) and the average relative deviation is $\bar{\varepsilon}_{Cd_2}=3.88\%$.

We build the fitting formulas for the average Nusselt Number Nu_1 and Nu_2 based on Eq. (5.1b), the fitting formula for spheroid-1 (leading particle) is given as

$$Nu_1=Q_1(\ell)Pr^{1/3}Re^{2/3}(Ar)^{c_1}+Q_2(\ell)Pr^{1/3}Re^{1/2}(Ar)^{c_2}+Q_3(\ell)(Ar)^{c_3}, \tag{5.6}$$

where $Q_i(\ell)=(a_i+b_i\ell)$, $i=1,2,3$.

Through a regression analysis, the unknown coefficients in Eqs. (5.6) are determined as $c_1=0.2004$, $c_2=0.1735$, $c_3=-0.1313$,

$$Q_1(\ell)=-0.0881+0.0074\ell, \tag{5.7a}$$
$$Q_2(\ell)=0.8134-0.0173\ell, \tag{5.7b}$$
$$Q_3(\ell)=1.3620+0.0488\ell. \tag{5.7c}$$

Quantitative comparisons can be found in Fig. 11(a) and the average relative deviation is $\bar{\varepsilon}_{Nu_1}=1.12\%$.

Similar to spheroid-1, the average Nusselt number for the spheroid-2 (trailing particle) is given as

$$Nu_2=Q_1(\ell)Pr^{1/3}Re^{2/3}(Ar)^{c_1}+Q_2(\ell)Pr^{1/3}Re^{1/2}(Ar)^{c_2}+Q_3(\ell)(Ar)^{c_3}, \tag{5.8}$$

where $Q_i(\ell)=(a_i+b_i\ell^{1/3}+d_i\ell^{1/2})$, $i=1,2,3$.

The unknown coefficients in Eq. (5.8) are determined as $c_1=-0.2347$, $c_2=0.3710$,

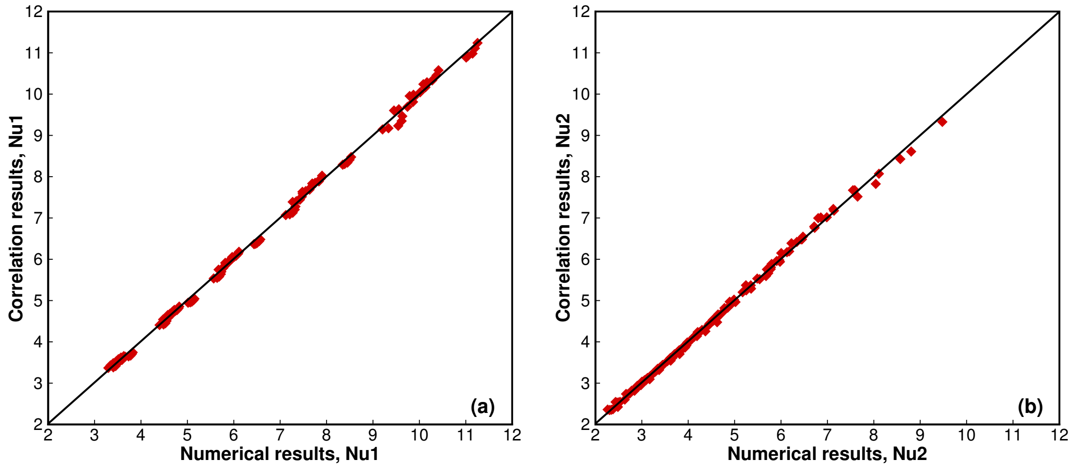

Figure 11: Parity plot of average Nusselt Number predicted using relations and corresponding calculations from numerical simulations. (a) Nu_1 from Eqs. (5.6) versus calculated Nu_1 and (b) Nu_2 from Eqs. (5.8) versus calculated Nu_2.

$c_3 = -0.1574$

$$Q_1(\ell) = -0.0490 + 0.1476\ell^{1/3} - 0.0748\ell^{1/2}, \tag{5.9a}$$

$$Q_2(\ell) = 0.1453 - 0.0519\ell^{1/3} + 0.1051\ell^{1/2}, \tag{5.9b}$$

$$Q_3(\ell) = -1.0681 + 5.0313\ell^{1/3} - 2.4942\ell^{1/2}. \tag{5.9c}$$

Quantitative comparisons can be found in Figs. 11(b) and the average relative deviation is $\bar{\varepsilon}_{Nu_2} = 1.0\%$.

5.4 Influence of the relative incidence angle

The force evolution and heat transfer of two tandem spheroids have been discussed in the previous subsections. The fundamental purpose of this subsection is to discuss the influence of the relative incidence angles on them, which has hardly been found in the literatures. As we all know, most particles immersed in the fluid are not parallel to each other. In other words, the relative position of the particles apart from the inter particle distance affects the configuration of the particles. To investigate this effect, we consider two relative incidence angles $\theta = 0°, 90°$ and $\phi = 0°, 90°$ as shown in Fig. 12. The cases when $Ar = 2.0$ from the previous 125 cases are selected, and the inter particle distance $L = 2.0D, 3.0D, 5.0D$ together with the Reynolds number $Re = 10, 100, 200$. Totally, 27 cases are studied.

The distribution of the non-dimensional fluid temperature as well as the streamlines around the two particles in the $X-Z$ plane at $Y = 5D$ are shown in Fig. 13, in which $Ar = 2.0$, $Re = 100$ and $2.0 \le L/D \le 5.0$. From Fig. 13(a1)-(c1), $\theta = 90°$ (corresponding to Fig. 12(b)), it can be found that the recirculation wake is very clear between the two

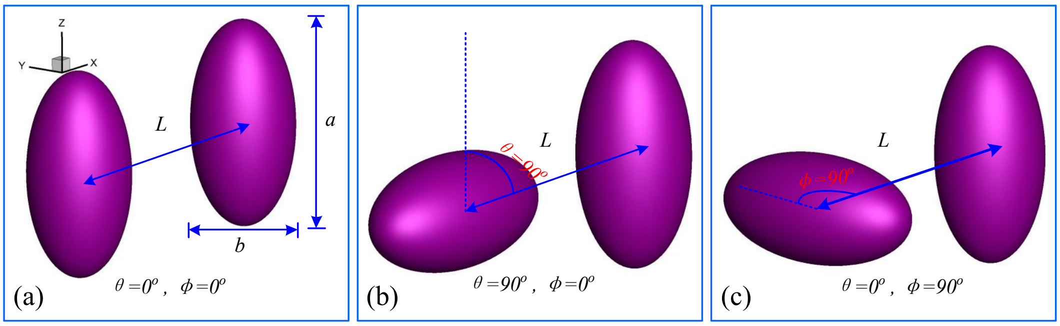

Figure 12: Particle size and relative incidence angle θ and ϕ.

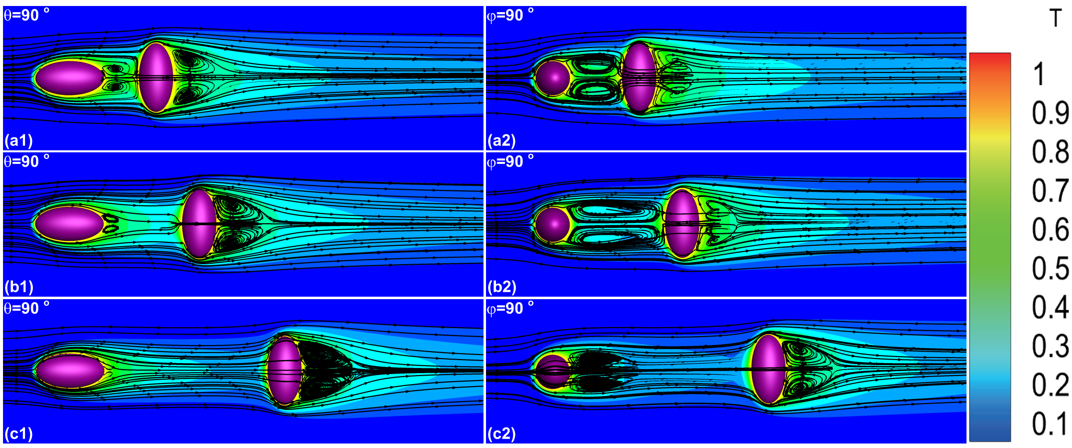

Figure 13: Temperature distributions and streamlines at $Ar=2.0$ and $Re=100$ ((a1), (a2): $L=2.0D$; (b1), (b2): $L=3.0D$; (c1), (c2): $L=5.0D$).

particles when $L/D=2.0$ but becomes weaker and weaker as the gap between the two particles increases (from Fig. 13(b1) to Fig. 13(c1)). This is due to the small frontal area of the leading particle and the strong resistance of the trailing one on the fluid under a very small inter particle distance $L/D=2.0$. As for Fig. 13(a2)-(c2), $\phi=90^\circ$ (corresponding to Fig. 12(c)), the frontal area of the leading particle is larger than Fig. 12(b) and when L/D=2.0, the surface distance between two particles is also larger than Fig. 12b. The flow separation behind both the two particles occurs for arbitrary values of the inter particle distance L. The length of the recirculation wake for $L/D=3.0$ is larger than that for L/D=2.0. When the inter particle distance continues to increase to L/D=5.0 (Fig. 13(c2)), the length of the recirculation wake decreases, which is almost unaffected by the trailing particle. On the contrary, the length of the recirculation wake of the trailing particle is becoming more and more obvious showing that the interaction between particles is weakened as the inter particle distance increases.

In summary, for a given Ar, when $\theta=90^\circ$, the recirculation wake behind the leading

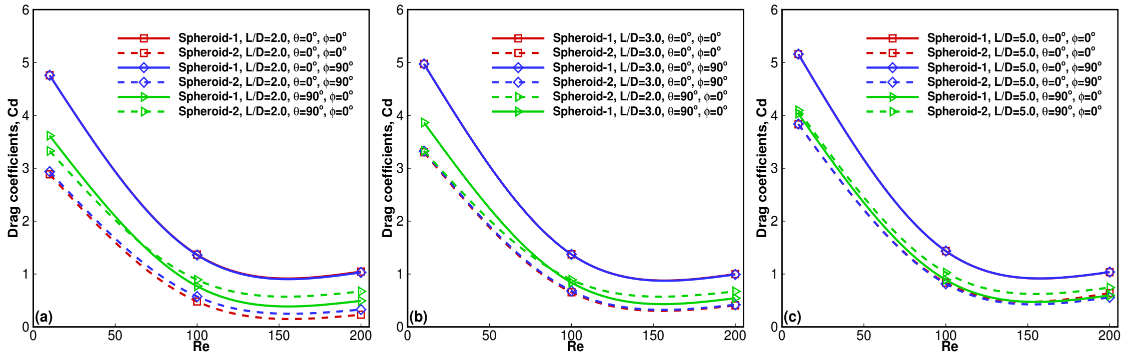

Figure 14: Effects of relative incidence angle θ and ϕ on the drag coefficients Cd of two tandem spheroid particles with different Re and L.

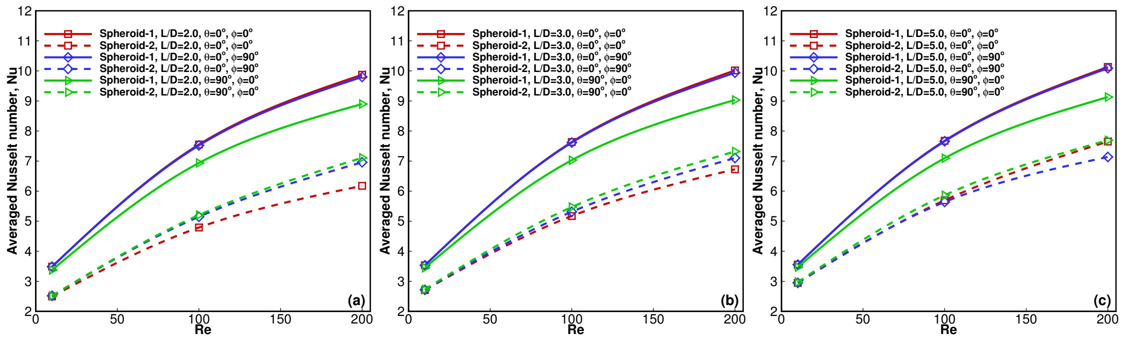

Figure 15: Effects of relative incidence angle θ and ϕ on the average Nusselt number Nu of two tandem spheroid particles with different Re and L.

particle decreases when L increases. But the recirculation wake behind the trailing particle is hardly affected by L. When $\phi=90°$, the recirculation wake behind the leading particle firstly increases but then decreases with the increase of L. The recirculation wake behind the trailing particle increases with L. This phenomenon shows that the inter particle distance L plays an important role in the two particle interaction both in the cases of $\theta=90°$ and $\phi=90°$. The effects of the relative incidence angle θ and ϕ and the inter particle distance L on fluid flow and heat transfer are described below. For the sake of simplicity, aspect ratio $Ar=2.0$ and inter particle distance $L/d=2.0,3.0,5.0$ are selected.

Fig. 14 shows the drag coefficients Cd at different Re and L under the same aspect ratio, quantitatively. Regardless of the relative incidence angle described by θ and ϕ and the gap between the particles described by the inter particle distance L, the drag coefficients for both leading particle Cd_1 and trailing particle Cd_2 decrease with the increase of Re. This finding is in line with the result of the previous discussion. It is also found that, when $\phi=90°$, the drag coefficient Cd_1 for the leading particle is almost unchanged under the same inter particle distance L. This phenomenon is not unexpected because no matter $\phi=0°$ or $\phi=90°$, the maximum axis is always perpendicular to the main flow direction (namely, frontal area of leading particle is same) and the effect of the trailing particle on the leading one is very slight. The same thing takes place on the drag coefficient of the trailing particle under the same conditions. But due to the small frontal area of the leading particle, its drag coefficient Cd_1 decreases when $\theta = 90°$. With the increase of the inter particle distance L, the difference between Cd_1 for leading particle and Cd_2 for trailing particle gradually decreases showing that the interaction between these two particles is weakened with the increase of the inter particle distance L.

Fig. 15 shows the average Nusselt number Nu at different Re and L under the same aspect ratio, quantitatively. Regardless of the relative incidence angles θ and ϕ and the inter particle distance L, the average Nusselt numbers for both the leading Nu_1 and trailing Nu_2 particles increase with Re. Irrespective of the Reynolds number Re and θ and ϕ, Nu_1 and Nu_2 increase with L. Similar to the drag coefficients, when $\phi = 90°$, Nu_1 and Nu_2 are hardly changed under the same inter particle distance L. But when $\theta = 90°$, Nu_1 decreases due to the small frontal area of the leading particle. At last, the difference between Nu_1 and Nu_2 is gradually decreasing with the increase of L.

6 Concluding remarks

In this study, the GPU based IB-LBM simulations are carried out to study the forced convection of two tandem spheroids. By changing the aspect ratio Ar, inter particle distance L between the solid particles and Reynolds number, the momentum exchange and heat transfer between the solid and fluid phases are quantitatively evaluated. The influence of the relative incidence angles is also discussed. Some notable findings are presented as follows:

The drag coefficients of both the two spheroids for a given aspect ratio Ar drop when increasing the Reynolds number Re, on the contrary, the average Nusselt numbers of both the two spheroids for a given aspect ratio Ar increase when increasing the Reynolds number Re. With the increase of the inter particle distance L, the interaction between particles is weakened and the drag coefficients and average Nusselt numbers for both the two spheroids increasing when increasing L, but they are all less than that of an isolated spheroid.

Based on the numerical results, the correlations for the drag coefficient and average Nusselt number are established by considering Re, Ar and L as the key influencing factors. The average relative deviations of the new correlations are $\bar{\varepsilon}_{Cd_1} = 1.62\%$ and $\bar{\varepsilon}_{Cd_2} = 3.88\%$ for the leading and trailing particles, respectively. The average relative deviations of the new correlations are $\bar{\varepsilon}_{Nu_1} = 1.12\%$ and $\bar{\varepsilon}_{Nu_2} = 1.0\%$ for the leading and trailing particles, respectively.

The relative incidence angles θ and ϕ play significant roles in influencing on the force evolution and heat transfer of the two spheroids. When $\phi = 90°$, the drag coefficient Cd_1 and average Nusselt number Nu_1 for the leading particle is hardly changed under the same inter particle distance L. But when $\theta = 90°$, the drag coefficient Cd_1 and average

Nusselt number Nu_1 decreases.

Nomenclature

α	LBM index (subscript)
$\breve{a},\breve{b},\breve{c}$	Principal semi-axes of ellipsoid along X-, Y- and Z-direction
Δs_l	Area that each Lagrangian point occupies on the particle surface
$\delta(\cdot)$	Delta function
δ_t	Fluid discrete time step
ℓ	Dimensionless inter particle distance ($\ell = L/D$)
ϵ	Solid volume fraction
κ	Thermal conductivity coefficient
λ_i	Parameters of fitting templet ($i=1,\cdots,6$)
$\mathbf{e}_{\boldsymbol{\alpha}}$	Lattice velocity
$\mathbf{F}_f$	External force on Lagrangian point
$\mathbf{r}$	Fluid space position vector
$\mathbf{u_f}$	Local fluid velocity
$\mathbf{u_s}$	Local particle velocity
$\mathbf{u}$	Fluid macro velocity
$\mathbf{X}_l$	Solid coordinate
ω_α	Fluid value of weight
ρ	Fluid macro density
τ_f	Fluid non-dimensional relaxation time of the density evolution
τ_g	Fluid non-dimensional relaxation time of the temperature evolution
$\mathbf{f}_d$	Drag force
θ,ϕ	Relative incident angle
$\tilde{T}_f$	Normalized fluid temperature

$\tilde{T}_s$	Normalized solid temperature
ε_{Nu}	Relative errors for average Nusselt number
ε_{Cd}	Relative errors for drag coefficient
A	Front area
Ar	Aspect ratio
c	Fluid lattice speed
c_s	Fluid lattice speed of sound
Cd	Drag coefficient
Cd_{avg}	New defined average drag coefficient ($Cd_{avg}=0.5[Cd_1+Cd_2]$)
D	Volume-equivalent sphere diameter
F_α	External force
f_α	Fluid density distribution function
f_α^{eq}	Fluid equilibrium density distribution function
F_x	Component of $\mathbf{F}_f$ in X-directions.
G_α	External heat source
g_α	Fluid temperature distribution function
g_α^{eq}	Fluid equilibrium temperature distribution function
h	Fluid mesh spacing
h_e	Convective heat transfer coefficient of the fluid
L	Inter particle distance
L_c	Characteristic length
Nu	Average Nusselt number
Nu_{avg}	New defined average Nusselt number ($Nu_{avg}=0.5[Nu_1+Nu_2]$)
Pr	Prandtl number
q	Heat flux
Re	Reynolds number

S Total area of the particle surface

T Fluid macro temperature

t Present time

T_c Low temperature

T_f Local fluid temperature

T_h High temperature

T_s Local particle temperature

u_0 Characteristic velocity

Acknowledgements

This work is financially supported by the National Science Foundation of China (Nos. 11571293, 51606040, 11501484, 11601462), the National Key R & D Program of China (No. 2016YFB0600101-4), Hunan Provincial Civil-Military Integration Industrial Development Project "Adaptive Multilevel Solver and Its Application in ICF Numerical Simulation", Jiangsu Province Science Foundation for Youths (No. BK20160677), and Hunan Provincial Innovation Foundation for Postgraduate (No. CX2016B246).

References

[1] C. K. CHEN, K. L. WONG AND S. C. LEE, *The finite element solution of laminar combined convection from two spheres in tandem arrangement*, Comput. Methods Appl. Mech. Eng., 59 (1986), pp. 73–84.
[2] R. C. CHEN AND Y. N. LU, *The flow characteristics of an interactive particle at low Reynolds numbers*, Int. J. Multiphase Flow, 25(8) (1999), pp. 1645–1655.
[3] R. C. CHEN AND J. L. WU, *The flow characteristics between two interactive spheres*, Chemical Eng. Sci., 55(6) (2000), pp. 1143–1158.
[4] T. S. CHEN AND A. MUCOGLU, *Analysis of mixed forced and free convection about a sphere*, Int. J. Heat Mass Transfer, 20(8) (1977), pp. 867–875.
[5] ZHI-GANG FENG AND EFSTATHIOS E. MICHAELIDES, *A numerical study on the transient heat transfer from a sphere at high Reynolds and Peclet numbers*, Int. J. Heat Mass Transfer, 43(2) (2000), pp. 219–229.
[6] A. GILMANOV, F. SOTIROPOULOS AND E. BALARAS, *A general reconstruction algorithm for simulating flows with complex 3D immersed boundaries on Cartesian grids*, J. Comput. Phys., 191(2) (2003), pp. 660–669.
[7] YANJUN GUAN, RODRIGO GUADARRAMA-LARA, XIAODONG JIA, KAI ZHANG AND DONGSHENG WEN, *Lattice Boltzmann simulation of flow past a non-spherical particle*, Adv. Powder Tech., 28(6) (2017), pp. 1486–1494.

[8] ANDREAS HÖLZER AND MARTIN SOMMERFELD, *Lattice Boltzmann simulations to determine drag, lift and torque acting on non-spherical particles*, Comput. Fluids, 38(3) (2009), pp. 572–589.

[9] XIAOYI HE, SHIYI CHEN AND GARY D DOOLEN, *A novel thermal model for the lattice Boltzmann method in incompressible limit*, J. Comput. Phys., 146(1) (1998), pp. 282–300.

[10] GHEORGHE JUNCU, *A numerical study of momentum and forced convection heat transfer around two tandem circular cylinders at low Reynolds numbers. Part I: Momentum transfer*, Int. J. Heat Mass Transfer, 50(19) (2007), pp. 3799–3808.

[11] GHEORGHE JUNCU, *A numerical study of momentum and forced convection heat transfer around two tandem circular cylinders at low Reynolds numbers: Part II: Forced convection heat transfer*, Int. J. Heat Mass Transfer, 50(19) (2007), pp. 3799–3808.

[12] GHEORGHE JUNCU, *Unsteady heat transfer from an oblate/prolate spheroid*, Int. J. Heat Mass Transfer, 53(17) (2010), pp. 3483–3494.

[13] CHUNHAI KE, SHI SHU, HAO ZHANG, HAIZHUAN YUAN AND DONGMIN YANG, *On the drag coefficient and averaged nusselt number of an ellipsoidal particle in a fluid*, Powder Tech., 325 (2018), pp. 134–144.

[14] INCHUL KIM, SAID ELGHOBASHI AND WILLIAM A. SIRIGNANO, *Three-dimensional flow over two spheres placed side by side*, J. Fluid Mech., 246(1) (1993), pp. 465–488.

[15] MOON KYOUNG KIM, KEON KIM DONG, SOON HYUN YOON AND DAE HEE LEE, *Measurements of the flow fields around two square cylinders in a tandem arrangement*, J. Mech. Sci. Tech., 22(2) (2008), pp. 397–401.

[16] NANDA KISHORE, *Flow and drag phenomena of pandem spheroid particles at finite Reynolds numbers*, Industrial Eng. Chemistry Res., 51(7) (2012), pp. 3186–3196.

[17] NANDA KISHORE, *Numerical investigation of interaction between spheroid particles in tandem arrangement at moderate Reynolds numbers*, Industrial Eng. Chemistry Res., 51(30) (2012), pp. 10265–10273.

[18] NANDA KISHORE AND SAI GU, *Momentum and heat transfer phenomena of spheroid particles at moderate Reynolds and Prandtl numbers*, Int. J. Heat Mass Transfer, 54(11) (2011), pp. 2595–2601.

[19] L. S. KLYACHKO, *Heat transfer between a gas and a spherical surface with the combined action of free and forced convection*, J. Heat Transfer, 85(4) (1963), pp. 355–357.

[20] H. KRUGGEL-EMDEN, B. KRAVETS, M. K. SURYANARAYANA AND R. JASEVICIUS, *Direct numerical simulation of coupled fluid flow and heat transfer for single particles and particle packings by a LBM-approach*, Powder Tech., 294 (2016), pp. 236–251.

[21] SHIYANG LI, JIAN YANG AND QIUWANG WANG, *Large eddy simulation of flow and heat transfer past two side-by-side spheres*, Appl. Thermal Eng., 121(C) (2017), pp. 810–819.

[22] S. C. LIANG, T. HONG AND L. S. FAN, *Effects of particle arrangements on the drag force of a particle in the intermediate flow regime*, Int. J. Multiphase Flow, 22(2) (1996), pp. 285–306.

[23] SAMUEL G. MUSONG, ZHI GANG FENG, EFSTATHIOS E. MICHAELIDES AND SHAOLIN MAO, *Application of a three dimensional immersed boundary method for free convection from single spheres and aggregates*, J. Fluids Eng., 138(4) (2016), pp. 331–336.

[24] X. D. NIU, C. SHU, Y. T. CHEW AND Y. PENG, *A momentum exchange-based immersed boundary-lattice Boltzmann method for simulating incompressible viscous flows*, Phys. Lett. A, 354(3) (2006), pp. 173–182.

[25] CHARLES S. PESKIN, *Numerical analysis of blood flow in the heart*, J. Comput. Phys., 25(3) (1977), pp. 220–252.

[26] L. PRAHL, A. HÖLZER AND D. ARLOV, *On the interaction between two fixed spherical particles*, Int. J. Multiphase Flow, 33(7) (2007), pp. 707–725.

[27] Y. H. Qian, D. D'Humières and P. Lallemand, *Lattice BGK models for Navier-Stokes equation*. Europhys. Lett., 17(6BIS) (1992), 479.

[28] W. E. Ranz, *Friction and transfer coefficients for single particles and packed beds*, Chemical Eng. Progress, 48 (1952), pp. 247–253.

[29] W. W. Ren, C. Shu, J. Wu and W. M. Yang, *Boundary condition-enforced immersed boundary method for thermal flow problems with Dirichlet temperature condition and its applications*, Comput. Fluids, 57 (2012), pp. 40–51.

[30] Andreas Richter and Petr A. Nikrityuk, *Drag forces and heat transfer coefficients for spherical, cuboidal and ellipsoidal particles in cross flow at sub-critical Reynolds numbers*, Int. J. Heat Mass Transfer, 55(4) (2012), pp. 1343–1354.

[31] Andreas Richter and Petr A. Nikrityuk, *New correlations for heat and fluid flow past ellipsoidal and cubic particles at different angles of attack*, Powder Technology, 249 (2013), pp. 463–474.

[32] L. W. Rong, K. J. Dong and A. B. Yu, *Lattice-Boltzmann simulation of fluid flow through packed beds of uniform spheres: Effect of porosity*, Chemical Eng. Sci., 99 (2013), pp. 44–58.

[33] P. N. Rowe and G. A. Henwood, *Drag forces in hydraulic model of a fluidized bed–Part I*, Trans. Inst. Chem. Eng., 39(01) (1961), pp. 41-45.

[34] A. Sohankar and A. Etminan, *Forced-convection heat transfer from tandem square cylinders in cross flow at low Reynolds numbers*, Int. J. Numer. Methods Fluids, 60(7) (2010), pp. 733–751.

[35] Reuven Tal, Dah Nain Lee and William A. Sirignano, *Heat and momentum transfer around a pair of spheres in viscous flow*, Int. J. Heat Mass Transfer, 27(11) (1984), pp. 1953–1962.

[36] H. Tavassoli, S. H. L. Kriebitzsch, M. A. Van Der Hoef, E. A. J. F. Peters and J. A. M. Kuipers, *Direct numerical simulation of particulate flow with heat transfer*, Int. J. Heat Fluid Flow, 31(6) (2010), pp. 1050–1057.

[37] H. Tavassoli, S. H. L. Kriebitzsch, M. A. van der Hoef, E. A. J. F. Peters and J. A. M. Kuipers, *Direct numerical simulation of particulate flow with heat transfer*, Int. J. Multiphase Flow, 57(2013), pp. 29–37.

[38] H. Tavassoli, E. A. J. F. Peters and J. A. M. Kuipers, *Direct numerical simulation of non-isothermal flow through dense bidisperse random arrays of spheres*, Powder Tech., 314 (20170, pp. 291–298.

[39] T. Tsuji, R. Narutomi, T. Yokomine, S. Ebara and A. Shimizu, *Unsteady three-dimensional simulation of interactions between flow and two particles*, Int. J. Multiphase Flow, 29(9) (2003), pp. 1431–1450.

[40] Yutaka Tsuji, Yoshinobu Morikawa and Kozo Terashima, *Fluid-dynamic interaction between two spheres*, Int. J. Multiphase Flow, 8(1) (1982), pp. 71–82.

[41] Huy Cong Vu, Jungkyu Ahn and Hwan Hwang Jin, *Numerical simulation of flow past two circular cylinders in tandem and side-by-side arrangement at low Reynolds numbers*, Ksce J. Civil Eng., 20(4) (2015), pp. 1–11.

[42] X. K. Wang, Z. Hao, J. X. Zhang and S. K. Tan, *Flow around two tandem square cylinders near a plane wall*, Exp. Fluids, 55(10) (2014), pp. 1–14.

[43] Dong Hyeog Yoon and Kyung Soo Yang, *Characterization of flow pattern past two spheres in proximity*, Phys. Fluids, 21(7) (2009), 098103.

[44] Xiaoqiang Yue, Hao Zhang, Chunhai Ke, Congshu Luo, Shi Shu, Yuanqiang Tan and Chunsheng Feng, *A GPU-based discrete element modeling code and its application in die filling*, Comput. Fluids, 110 (2015), pp. 235–244.

[45] T. Yuge, *Experiments on heat transfer from spheres including combined natural and forced convection*, J. Heat Transfer, 82(3) (1960), pp. 214–220.

[46] MARIAN ZASTAWNY, GEORGE MALLOUPPAS, FAN ZHAO AND BEREND VAN WACHEM, *Derivation of drag and lift force and torque coefficients for non-spherical particles in flows*, Int. J. Multiphase Flow, 39 (2012), pp. 227–239.

[47] WENQI ZHONG, AIBING YU, XUEJIAO LIU, ZHENBO TONG AND HAO ZHANG, *DEM/CFD-DEM modelling of non-spherical particulate systems: Theoretical Developments and Applications*, Powder Tech., 302 (2016), pp. 108–152.

[48] C. ZHU, S. C. LIANG AND L. S. FAN, *Particle wake effects on the drag force of an interactive particle*, Int. J. Multiphase Flow, 20(1) (1994), pp. 117–129.